water

MDPI

Article

Bragg Scattering of Surface Gravity Waves Due to Multiple Bottom Undulations and a Semi-Infinite Floating Flexible Structure

Prakash Kar [1], Santanu Koley [2], Kshma Trivedi [2] and Trilochan Sahoo [3,*]

[1] Department of Statistics, Midnapore College, Midnapore 721101, India; pkprakash47@gmail.com
[2] Department of Mathematics, Birla Institute of Technology and Science-Pilani, Hyderabad Campus, Hyderabad 500078, Telangana, India; santanukoley1989@gmail.com (S.K.); p20190439@hyderabad.bits-pilani.ac.in (K.T.)
[3] Department of Ocean Engineering and Naval Architecture, Indian Institute of Technology Kharagpur, Kharagpur 721302, India
* Correspondence: tsahoo1967@gmail.com or tsahoo@naval.iitkgp.ac.in

Abstract: Surface gravity wave interaction with a semi-infinite floating elastic plate in the presence of multiple undulations has been studied under the assumption of linearized water wave theory and small amplitude structural response. The elastic plate is modeled using the Euler-Bernoulli beam equation, whilst the multiple undulations are categorized as an array of submerged trenches or breakwaters. The numerical solution obtained in finite water depth using the boundary element method is validated with the semi-analytic solution obtained under shallow water approximation. Bragg resonance occurs due to the scattering of surface waves by an array of trenches or breakwaters irrespective of the presence of the floating semi-infinite plate. The zero-minima in wave reflection occur when the width of the trench and breakwater is an integer multiple of 0.6 and 0.35 times wavelength, respectively, as the number of trenches or breakwaters increases. In contrast to trenches and breakwaters in isolation, non-zero minima in wave reflection occur in the presence of a semi-infinite plate. Moreover, the number of complete cycles in trenches is less than the number of complete cycles in breakwaters, irrespective of the presence of the floating structure. The frequency of occurrence of zero minimum in wave reflection is reduced in the presence of the semi-infinite plate, and wave reflection increases with an increase in rigidity of the floating plate. Time-dependent simulation of free surface displacement and plate deflection due to multiple undulations of seabed in the presence of the semi-infinite floating plate is demonstrated in different cases.

Keywords: Bragg reflection; trenches; breakwaters; semi-infinite plate; Gaussian wave packet

Citation: Kar, P.; Koley, S.; Trivedi, K.; Sahoo, T. Bragg Scattering of Surface Gravity Waves Due to Multiple Bottom Undulations and a Semi-Infinite Floating Flexible Structure. *Water* **2021**, *13*, 2349. https://doi.org/10.3390/w13172349

Academic Editors: Mariano Buccino and Alistair Borthwick

Received: 7 June 2021
Accepted: 20 August 2021
Published: 27 August 2021

1. Introduction

One of the challenges due to global warming is the rise in sea level contributing to coastal flooding and erosion. Very large floating structures (VLFS), in the form of semi-infinite floating structures, have been introduced as an eco-friendly solution to meet the need for land space. These structures are very large in nature and deform elastically under wave action. During the last two decades, for different serviceability conditions, several techniques have been proposed for mitigating wave-induced structural responses on floating structures. Recent progress on the performance of anti-motion systems for reducing wave forces on the VLFSs was reviewed by Wang et al. [1]. An analogous discipline is the wave-ice interaction problems in which the ice sheet is modeled as an elastic plate. Meylan and Squire [2] analyzed the scattering of surface waves by a single ice floe. Sahoo et al. [3] studied the scattering of surface gravity waves by a semi-infinite floating elastic plate and analyzed the role of different types of edge conditions on the vibration of the floating structure. Squire [4] reviewed the synergy between a floating ice sheet and a very large floating structure in the study of surface gravity wave interaction with a floating elastic

plate. Sturova [5] investigated the unsteady response of a heterogeneous elastic plate under shallow water approximation. Bhattacharjee and Soares [6] studied the transformation of the flexural gravity waves by a vertical wall. Papathanasiou et al. [7] studied the unsteady hydroelastic response of a floating ice shelf under long-wave excitation using the finite element method. Sturova [8] investigated the hydroelastic response of an external load moving over a semi-infinite ice sheet in the sub-critical regime. Das et al. [9] investigated the blocking dynamics of flexural gravity waves in the presence of ocean current and compression. Barman et al. [10] studied the flexural gravity wave scattering due to a crack in a floating ice sheet in the context of blocking dynamics. Jiang et al. [11] designed and analyzed the floating prestressed concrete structures in shallow waters. Kalyanaraman et al. [12] investigated the shallow-water limit for the modeling of wave-induced ice-shelf vibrations. Various developments of numerical algorithms on ice-water-structure interaction was reviewed by Ni et al. [13].

In recent decades, due to the advent of computational techniques, significant progress on the study of scattering of gravity waves by VLFS over undulated seabed has been witnessed in the literature. Belibassakis and Athanassoulis [14] analyzed the hydroelastic responses of a VLFS floating over the undulated seabed. Karmakar et al. [15] investigated the role of multi-step bottom topography on the transformation of flexural gravity waves in finite water depth. Karperaki et al. [16] analyzed the transient hydroelastic response of a flexible floating plate, which is connected to the seabed elastically. The study of Kar et al. [17] reveals that the maximal peak Bragg reflection curve is nearly linear in the case of long wave scattering by a pair of submerged trenches, whilst the pattern of the said curves appears to be non-linear in the case of an array of finite number of submerged trenches. Kar et al. [18] studied the scattering of long gravity waves due to an array of submerged trenches and breakwaters in the presence of an array of floating flexible plates.

The boundary element method (BEM) is broadly used for dealing with varieties of physical problems associated with wave-structure interactions. Koley [19] used a coupled boundary element-finite difference method to study the effect of undulated bottom on the Bragg scattering of water waves by a flexible floating plate of finite length. Vijay et al. [20] used the boundary element method to reduce the wave-induced responses of a floating structure near a wall in the presence of permeable plates. Mohapatra et al. [21] developed the multi-domain BEM method to study the scattering of gravity waves by a submerged wavy porous plate. Ray et al. [22] investigated the water wave scattering by a submerged thick rectangular barrier in the presence of an ice sheet. Gayathri et al. [23] studied the wave scattering obliquely by a floating rigid bridge placed near a vertical porous and flexible barrier. Recently, Vita et al. [24] studied the interaction of surface gravity waves with an array of submerged periodic structures for attenuating wave height. However, there is no study in the literature on wave interaction with a semi-infinite floating flexible in the presence of multiple seabed undulations.

In the present study, Bragg scattering of surface gravity waves by an array of submerged trenches and breakwaters is analyzed in the presence of a semi-infinite floating flexible plate. Various results associated with the long gravity waves obtained via the analytic method are validated with the numerical results computed based on the boundary element method. Moreover, energy identity is derived and used to check the accuracy of the results. Various physical quantities, such as reflection coefficients, plate deflection, and free surface elevations, are computed for analyzing the effects of different physical parameters associated with wave motion, trenches, breakwaters, and floating semi-infinite plate. The Bragg reflection patterns generated due to various combinations of trenches/breakwater and the semi-infinite floating plate are analyzed. The wave packets interacting with an array of trenches or breakwaters are demonstrated in the presence/absence of the semi-infinite plate.

2. Mathematical Formulation

The problem of surface gravity wave interaction with a semi-infinite floating plate in the presence of multiple bottom undulations is studied in the two dimensions in the Cartesian coordinate system. Here, $x-$axis is taken along the horizontal direction, and $y-$axis is directed vertically downward. There is an array of N rectangular trenches or breakwaters of equal width w, with the gap between the leading edges of two adjacent trenches/breakwaters being d, which occupy the regions $x_{j,1} < x \leq x_{j,2}\ (= x_{j,1} + w)$ for $j = 1, 2, 3, \ldots, N$. The floating semi-infinite plate occupies the region $p \leq x < \infty,\ \ y = 0$, and L_g is the gap length between the plate and the lee-side of the rightmost N^{th} trench or breakwater. The water depth at the sea-side and shore-side of the trenches is h_1, whereas the water depth within the submerged breakwaters is h_2 with $h_1 > h_2$, as shown in Figure 1. On the other hand, it may be noted that, in the case of submerged trenches, h_1 will be less than h_2. Moreover, the water depth in-between the trenches and the plate covered region is considered to be h_1. Under the assumptions of small amplitude surface gravity wave theory with motion being simple-harmonic motion in time with angular frequency ω, the velocity potential $\Phi_j(x, y, t)$ is written as $\Phi_j(x, y, t) = \Re\{\phi_j(x, y)e^{-i\omega t}\}$, with subscripts 1 and 2 corresponding to the open water and the plate covered regions, respectively. Further, the free surface elevation $\zeta(x, t)$ and the plate deflection $\tau(x, t)$ take the form $\zeta(x, t) = \Re\{\eta(x)e^{-\mathrm{i}\omega t}\}$, $\tau(x, t) = \Re\{\nu(x)e^{-\mathrm{i}\omega t}\}$, where $\eta(x)$ and $\nu(x)$ are the spatial components of the free surface elevation and plate deflection, respectively. Thus, the spatial components of the velocity potentials $\phi_j(x, y)$ (for $j = 1, 2$) satisfy the Laplace equation.

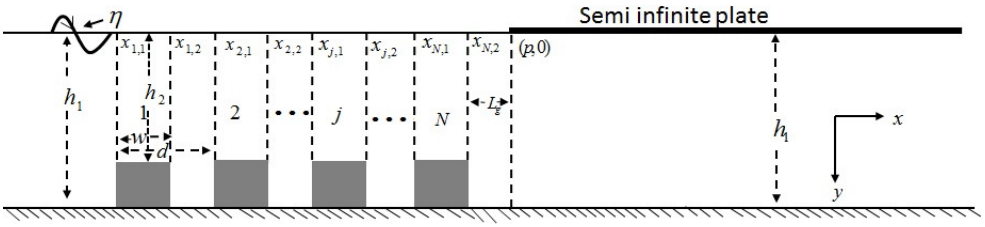

Figure 1. Schematic of wave motion over undulated bed and floating elastic plate.

$$\left(\frac{\partial^2}{\partial x^2} + \frac{\partial^2}{\partial y^2}\right)\phi_j = 0. \tag{1}$$

The free surface condition in the open water region is given by

$$\frac{\partial \phi_1}{\partial y} + K\phi_1 = 0, \ \text{ on } \ y = 0, \ \ -\infty < x < p, \tag{2}$$

where $K = \omega^2/g$ is the wavenumber associated with the surface gravity waves in infinite water depth. Further, on the plate covered surface, the linearized dynamic boundary condition yields (see Stoker [25] and Kar et al. [18] for details)

$$EI\nu_{xxxx} + \left(\rho g - m_s\omega^2\right)\nu = -\mathrm{i}\rho\omega\phi_2, \ \text{ on } \ y = 0, \ p < x < \infty, \tag{3}$$

with E being the Young's modulus and $I = d_s^3/(12(1-\nu^2))$, d_s being the plate thickness, ν being the Poisson's ratio, $m_s = \rho_s d_s$ being the uniform mass of the plate per unit length, and ρ_s being the density of the plate. The linearized free surface kinematic boundary condition on the elastic plate is given by

$$\frac{\partial \phi_2}{\partial y} = -\mathrm{i}\omega\nu, \ \text{ on } \ y = 0, \ p < x < \infty. \tag{4}$$

The free edge condition of the semi-infinite plate at $x = p$ yields

$$\nu_{xx} = 0, \quad \nu_{xxx} = 0, \text{ at } x = p, \ y = 0. \tag{5}$$

On the other, the boundedness of the solution at $x \to \infty$ yields

$$\nu(x) \to \text{finite value}, \text{ at } x \to \infty. \tag{6}$$

The boundary condition on the rigid bottom yields

$$\frac{\partial \phi_j}{\partial n} = 0, \text{ on } y = h(x), \tag{7}$$

where $\partial/\partial n$ represent the normal derivative. In Equation (7), the bottom boundary $h(x)$ takes the form

$$h(x) = \begin{cases} h_1, \text{ for } \{x < x_{1,1}\} \cup \{x > x_{N,2}\} \cup \{x_{j,2} < x < x_{j+1,1}\} \\ \qquad\qquad (j = 1, 2, \cdots, N-1), \\ h_2, \text{ for } \{x_{j,1} \le x \le x_{j,2}\} (j = 1, 2, \cdots, N). \end{cases} \tag{8}$$

Finally, the far-field radiation conditions are of the forms

$$\begin{cases} \phi_1(x,y) \to \phi^I(x,y) + A_R \, \phi^I(-x,y), \text{ as } x \to -\infty, \\ \phi_2(x,y) \to A_T \, \psi(x,y), \text{ as } x \to \infty, \end{cases} \tag{9}$$

where $\phi^I(x,y) = \dfrac{\cosh(k_1(h_1 - y))}{\cosh(k_1 h_1)} e^{ik_1 x}$ is the incident wave velocity potential, with k_1 being the positive real root of the dispersion relation $\omega^2 = gk \tanh(kh_1)$. Further, $\psi(x,y) = \dfrac{\cosh(p_1(h_1 - y))}{\cosh(p_1 h_1)} e^{ip_1 x}$, with p_1 being the positive real root of the dispersion relation

$$p\left\{\left(\rho g - m_s \omega^2\right) + Dp^4\right\} \tanh ph_1 = \rho g - m_s \omega^2, \tag{10}$$

with $D = EI$ being the rigidity of the semi-infinite plate. It is to be noted that A_R and A_T are the unknown constants associated with the reflection and transmission coefficients. To incorporate the far-field boundary conditions as in Equation (9) in the boundary element method, the alternate form of the radiation condition will be used is given by

$$\begin{cases} \dfrac{\partial(\phi_1 - \phi^I)}{\partial x} + ik_1\left(\phi_1 - \phi^I\right) = 0, \text{ as } x \to -\infty, \\ \dfrac{\partial \phi_2}{\partial x} - ip_1 \phi_2 = 0, \qquad\qquad \text{as } x \to \infty. \end{cases} \tag{11}$$

3. Numerical Solution Based on Boundary Element Method

Here, the boundary value problem, as discussed in Section 2, is handled for a solution using the boundary element method (BEM). In BEM, all the boundary conditions except the plate surface condition can be easily incorporated. To use the plate surface boundary conditions (3)–(6), the normal velocity $\partial\phi_2/\partial n$ is written in terms of the velocity potential ϕ_2 along the plate covered surface. Thus, the plate dynamic boundary condition (3) is rewritten as

$$\frac{d^4 \nu}{dx^4} + \left(\frac{\rho g - m_s \omega^2}{D}\right) \nu = \frac{-i\rho\omega\phi_2}{D}. \tag{12}$$

The characteristic polynomial of Equation (12) can be written as

$$r^4 + C = 0, \tag{13}$$

where $C = \left(\frac{\rho g - m_s\omega^2}{D}\right)$. As $\rho g >> m_s\omega^2$, Equation (13) will have four complex conjugate roots in four quadrants of the form $\pm\delta_j$ for $j = 1, 2$ with $\delta_1 = a + \mathrm{ib}$, $\delta_2 = a - \mathrm{ib}$ $\mathrm{a}, \mathrm{b} > 0$. Now, the Green's function associated with Equation (12) takes the form

$$g_p(x,\xi) = \begin{cases} a_1 e^{\delta_1 x} + b_1 e^{-\delta_1 x} + c_1 e^{\delta_2 x} + d_1 e^{-\delta_2 x}, & x < \xi, \\ a_2 e^{\delta_1 x} + b_2 e^{-\delta_1 x} + c_2 e^{\delta_2 x} + d_2 e^{-\delta_2 x}, & x > \xi, \end{cases} \tag{14}$$

where ξ is the source point, and x is the field point on the plate boundary, and satisfies the following properties

$$\begin{cases} g_p(x,\xi) \text{ is bounded as } x \to \infty, \\ \left.\dfrac{\partial^2 g_p}{\partial x^2}\right|_{x=p} = \left.\dfrac{\partial^3 g_p}{\partial x^3}\right|_{x=p} = 0, \\ g_p,\ \dfrac{\partial g_p}{\partial x} \text{ and } \dfrac{\partial^2 g_p}{\partial x^2} \text{ are continuous at } x = \xi, \\ \left.\dfrac{\partial^3 g_p}{\partial x^3}\right|_{x=\xi^+} - \left.\dfrac{\partial^3 g_p}{\partial x^3}\right|_{x=\xi^-} = -1. \end{cases} \tag{15}$$

The unknowns in Equation (14) are computed by solving the following matrix system

$$\begin{bmatrix} e^{\delta_1\xi} & e^{-\delta_1\xi} & e^{\delta_2\xi} & e^{-\delta_2\xi} & -e^{-\delta_1\xi} & -e^{-\delta_2\xi} \\ \delta_1 e^{\delta_1\xi} & -\delta_1 e^{-\delta_1\xi} & \delta_2 e^{\delta_2\xi} & -\delta_2 e^{-\delta_2\xi} & \delta_1 e^{-\delta_1\xi} & \delta_2 e^{-\delta_2\xi} \\ \delta_1^2 e^{\delta_1\xi} & \delta_1^2 e^{-\delta_1\xi} & \delta_2^2 e^{\delta_2\xi} & \delta_2^2 e^{-\delta_2\xi} & -\delta_1^2 e^{-\delta_1\xi} & -\delta_2^2 e^{-\delta_2\xi} \\ -\delta_1^3 e^{\delta_1\xi} & \delta_1^3 e^{-\delta_1\xi} & -\delta_2^3 e^{\delta_2\xi} & \delta_2^3 e^{-\delta_2\xi} & -\delta_1^3 e^{-\delta_1\xi} & -\delta_2^3 e^{-\delta_2\xi} \\ \delta_1^2 e^{\delta_1 p} & \delta_1^2 e^{-\delta_1 p} & \delta_2^2 e^{\delta_2 p} & \delta_2^2 e^{-\delta_2 p} & 0 & 0 \\ \delta_1^3 e^{\delta_1 p} & -\delta_1^3 e^{-\delta_1 p} & \delta_2^3 e^{\delta_2 p} & -\delta_2^3 e^{-\delta_2 p} & 0 & 0 \end{bmatrix} \begin{bmatrix} a_1 \\ b_1 \\ c_1 \\ d_1 \\ b_2 \\ d_2 \end{bmatrix} = \begin{bmatrix} 0 \\ 0 \\ 0 \\ -1 \\ 0 \\ 0 \end{bmatrix}, \tag{16}$$

along with $a_2 = c_2 = 0$. Using Equation (14) into Equation (12), the plate deflection $\nu(x)$ can be written as

$$\nu(x) = -\frac{\mathrm{i}\rho\omega}{D} \int_p^\infty g_p(x,\xi)\ \phi_2(\xi) d\xi. \tag{17}$$

Finally, substituting the expression of $\nu(x)$ as in Equation (17) into Equation (4), we get

$$\frac{\partial \phi_2}{\partial y} = -\frac{\rho\omega^2}{D} \int_p^\infty g_p(x,\xi)\ \phi_2(\xi) d\xi. \tag{18}$$

Introducing the operator

$$\mathcal{G}(f(x)) = -\frac{\rho\omega^2}{D} \int_p^\infty g_p(x,\xi)\ f(\xi) d\xi, \tag{19}$$

Equation (18) can be written as

$$\frac{\partial \phi_2}{\partial y} = \mathcal{G}(\phi_2(x)). \tag{20}$$

This particular form will be used in the BEM formulation at a later stage. Now, using Green's second identity to the functions $\phi(x,y)$ and $G(x,y;x_0,y_0)$ in the region Ω bounded by Γ, it is derived that

$$\frac{1}{2}\phi(x,y) = \int_\Gamma \left(\phi(x_0,y_0)\frac{\partial G(x,y;x_0,y_0)}{\partial n} - G(x,y;x_0,y_0)\frac{\partial \phi(x_0,y_0)}{\partial n}\right) d\Gamma(x_0,y_0), \quad \text{for } (x,y) \in \Gamma. \tag{21}$$

In Equation (21), $G(x,y;x_0,y_0)$ is the free space Green's function, which satisfies

$$\left(\frac{\partial^2}{\partial x^2} + \frac{\partial^2}{\partial y^2}\right) G = \delta(x-x_0)\delta(y-y_0), \tag{22}$$

and takes the form $G(x,\, y\,;\, x_0,\, y_0) = (1/2\pi)\ln r$, where $r = \sqrt{(x-x_0)^2 + (y-y_0)^2}$ represents the distance between the field point (x,y) and the source point (x_0,y_0). Using the boundary conditions (2), (7), (11), and (20) into the integral Equation (21), we obtain

$$\begin{aligned} C\phi \;+\; & \int_{\Gamma_l}\left(\frac{\partial G}{\partial n} - \mathrm{i}k_1 G\right)\phi d\Gamma + \int_{\Gamma_b}\phi\frac{\partial G}{\partial n}d\Gamma + \int_{\Gamma_r}\left(\frac{\partial G}{\partial n} - \mathrm{i}p_1 G\right)\phi d\Gamma + \int_{\Gamma_p}(\phi\frac{\partial G}{\partial n} \\ -\; & G\mathcal{G}(\phi))d\Gamma + \int_{\Gamma_f}\left(\frac{\partial G}{\partial n} + KG\right)\phi d\Gamma = \int_{\Gamma_l}\left(\frac{\partial \phi^I}{\partial n} - \mathrm{i}k_1\phi^I\right)G d\Gamma, \end{aligned} \tag{23}$$

where C is a constant which depends on the interior angle between the linear boundary elements. In Equation (23), Γ_l and Γ_r are the auxiliary boundaries situated at the far-field, as shown in Figure 2. These two auxiliary boundaries are taken sufficiently far away in both sides so that Equation (11) holds. Further, Γ_b, Γ_p, and Γ_f represent the bottom boundary, plate covered surface, and the free surface, respectively. The details derivation for reducing Equation (23) into system of equations are provided in the Appendix A. Next, the influence coefficients, as defined in the Appendix A, are calculated analytically when the field points match with that of the source points, whilst the Gaussian quadrature formula is used otherwise (see Katsikadelis [26] for details). Subsequently, using the collocation method, a linear algebraic system of equations is obtained, which is handled for the solution. Next, using Equation (9), the reflection coefficient K_r and transmission coefficient K_t are obtained using the formulae given by

$$K_r = |A_R| = \left|\phi_1(x,0) - e^{\mathrm{i}k_1 x}\right|_{x=-\infty}, \tag{24}$$

$$K_t = \frac{p_1}{k_1}\frac{\tanh(p_1h_1)}{\tanh(k_1h_1)}|A_t| = \frac{p_1}{k_1}\frac{\tanh(p_1h_1)}{\tanh(k_1h_1)}\left|\phi_2(x,o)\right|_{x=\infty}, \tag{25}$$

where $\phi_1(-\infty,0)$ and $\phi_2(\infty,0)$ correspond to the left and right most panel on the boundary Γ_f, respectively.

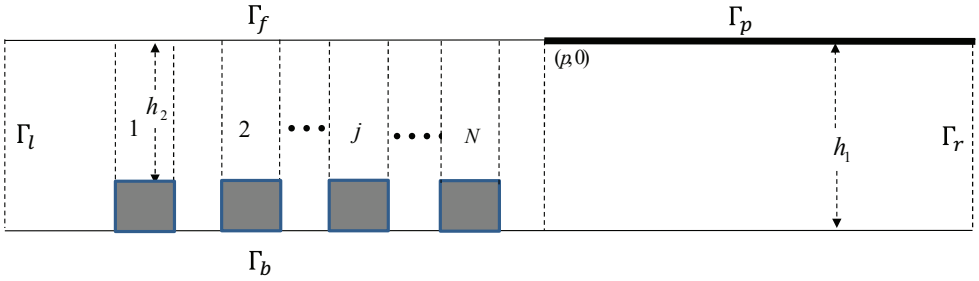

Figure 2. Computational domain for BEM.

4. Energy Identity

Here, the energy balance relation is derived for the physical problem discussed in Section 2 using the procedure adopted in Evans and Davies [27]. To derive the energy balance relation, Green's second identity is applied to the functions $\phi(x,y)$ and its complex conjugate $\bar{\phi}(x,y)$ over the region bounded by the lines $\Gamma_l \cup \Gamma_b \cup \Gamma_r \cup \Gamma_p \cup \Gamma_f$. The contribution from the line Γ_l as $x \to -\infty$ is given by

$$\mathrm{i}\left(1-|A_R|^2\right)\ \frac{2k_1h_1+\sinh(2k_1h_1)}{2\cosh^2(k_1h_1)}. \tag{26}$$

No contribution will come from Γ_b and Γ_f. The contribution from Γ_p as $x \to \infty$ is given by

$$-\frac{4\mathrm{i}\ Dp_1^4\tanh(p_1h_1)}{\left(Dp_1^4+(\rho g-m_s\omega^2)\right)}|A_T|^2. \tag{27}$$

Now, the contribution from Γ_r as $x \to \infty$ is given by

$$-\,\mathrm{i}\,|A_T|^2\ \frac{2p_1h_1+\sinh(2p_1h_1)}{2\cosh^2(p_1h_1)}. \tag{28}$$

Adding all the terms, the energy balance relation is obtained as

$$|A_R|^2+|A_T|^2\left(\frac{\chi_2}{\chi_1}+\frac{4Dp_1^4\tanh(p_1h_1)}{\left(Dp_1^4+(\rho g-m_s\omega^2)\right)\chi_1}\right)=1, \tag{29}$$

where χ_j for $j=1,2$ are given by

$$\chi_1=\frac{2k_1h_1+\sinh(2k_1h_1)}{2\cosh^2(k_1h_1)},\quad \chi_2=\frac{2p_1h_1+\sinh(2p_1h_1)}{2\cosh^2(p_1h_1)}. \tag{30}$$

Now, using the definition of K_r and K_t as defined in Equation (24), the energy identity in Equation (29) can be rewritten as

$$K_r^2+\gamma K_t^2=1, \tag{31}$$

where $\gamma=\dfrac{k_1}{p_1}\dfrac{\sinh(2k_1h_1)}{\sinh(2p_1h_1)}\times\dfrac{\left(Dp_1^4+(\rho g-m_s\omega^2)\right)2p_1h_1+\left(5Dp_1^4+(\rho g-m_s\omega^2)\right)\sinh(2p_1h_1))}{\rho g(2k_1h_1+\sinh(2k_1h_1))}$.

The energy identity as obtained in Equation (31) is equivalent to the one defined in Karmakar et al. [15] in case of normalized incident wave.

5. Analytic Long Wave Solution

In this section, Bragg scattering of small amplitude long waves due to multiple bottom undulations in the presence of the semi-infinite floating ice sheet is studied analytically, as shown in Figure 1. Assuming the motion as time-harmonic in time with angular frequency ω, the velocity potential $\Phi(x,t)$ is written in the form $\Phi(x,t)=\Re\{\phi(x)e^{-\mathrm{i}\omega t}\}$. Further, the free surface elevation in the open water region $\zeta(x,t)$ and the plate deflection $\tau(x,t)$ are written in the forms $\zeta(x,t)=\Re\{\eta(x)e^{-\mathrm{i}\omega t}\}$, $\tau(x,t)=\Re\{\nu(x)e^{-\mathrm{i}\omega t}\}$, with $\eta(x)$ and $\nu(x)$ being the spatial components of the free surface elevation and plate deflection, respectively. In the presence of the submerged trenches and the floating plate, the spatial component of the velocity potential ϕ can be divided into two parts, ϕ_1 (velocity potential in the open water region) and ϕ_2 (velocity potential in the plate covered region).

The long wave equation in the open water region in term of $\phi_1(x)$ is given by (see Kar et al. [18] and Sahoo [28] for details)

$$\phi_{1xx}+k_j^2\phi_1=0, \tag{32}$$

where $k_j^2 = \omega^2/gh_j$ for $j = 1,\ 2$.
Hence, the solution of Equation (32) in the open water region (without semi-infinite plate covered region) is of the form

$$\phi_1(x) = \begin{cases} e^{ik_1(x-x_{1,1})} + A_R e^{-ik_1(x-x_{1,1})} & \text{for } x \le x_{1,1}, \\ A_1^j e^{ik_2(x-x_{j,2})} + A_2^j e^{-ik_2(x-x_{j,2})} & \text{for } x_{j,1} \le x \le x_{j,2},\ j = 1,2,3,..,N \\ B_1^j e^{ik_1(x-x_{j+1,1})} + B_2^j e^{-ik_1(x-x_{j+1,1})} & \text{for } x_{j,2} \le x \le x_{j+1,1}, \\ & j = 1,2,3,..,N-1 \\ C_1 e^{ik_1(x-p)} + C_2 e^{-ik_1(x-p)} & \text{for } x_{N,2} \le x \le p, \end{cases} \tag{33}$$

where A_R is the unknown constant associated with the reflection coefficient, and A_t^j, B_t^j, C_t are the unknown constants for $t = 1,\ 2$ and $j = 1,2,\ldots.N$. The linearized long wave equation in the plate covered region in term of the spatial component $\phi_2(x)$ is given by (see Kar et al. [18])

$$\frac{d^6\phi_2}{dx^6} + \frac{\rho g - m_s\omega^2}{D}\frac{d^2\phi_2}{dx^2} + \frac{\omega^2\rho}{Dh_1}\phi_2 = 0. \tag{34}$$

Hence, the solution of Equation (34) in the semi-infinite plate-covered region (see Kalyanaraman et al. [12]) is of the form

$$\phi_2(x) = D^1 e^{m_4(x-p)} + D^2 e^{m_3(x-p)} + D^3 e^{m_5(x-p)},\ \ p < x < \infty, \tag{35}$$

where $D^k,\ k = 1,2,3$ are unknown constants to be computed, and $m_i (i = 1,...,6)$ are the roots in m of the characteristic polynomial

$$m^6 + \frac{\rho g - m_s\omega^2}{D}m^2 + \frac{\omega^2\rho}{Dh_1} = 0, \tag{36}$$

which are of the form $m_{1,2} = \delta \pm i\sigma$, $m_{3,4} = -\delta \pm i\sigma$, $m_{5,6} = \pm i\xi$ with $\delta, \sigma \in \mathbb{R}_+$, $\xi \in \mathbb{R}_+$. The free edge condition of semi-infinite plate at $x = p$ yields

$$\frac{\partial^4\phi_2}{\partial x^4}\Big|_{x=p} = 0,\ \ \frac{\partial^5\phi_2}{\partial x^5}\Big|_{x=p} = 0. \tag{37}$$

Using Equation (35) in Equation (37), we have

$$D^1 = \frac{m_5 - m_3}{m_3 - m_4}\left(\frac{m_5}{m_4}\right)^4 D^3 \ \text{ and } \ D^2 = \frac{m_4 - m_5}{m_3 - m_4}\left(\frac{m_5}{m_3}\right)^4 D^3.$$

Hence, Equation (35) converts into

$$\phi_2(x) = \left(\frac{m_5 - m_3}{m_3 - m_4}\left(\frac{m_5}{m_4}\right)^4 e^{m_4(x-p)} + \frac{m_4 - m_5}{m_3 - m_4}\left(\frac{m_5}{m_3}\right)^4 e^{m_3(x-p)} + e^{m_5(x-p)}\right) D^3. \tag{38}$$

Thus, from Equations (32) and (38), the velocity potential ϕ in the fluid domain can be expressed as

$$\phi(x) = \begin{cases} \phi_1(x) & \text{for } x_{1,1} \le x \le p, \\ \phi_2(x) & \text{for } p \le x < \infty. \end{cases} \tag{39}$$

The continuity of mass flux and pressure across the interfaces $x = \tilde{x}$ yield

$$\phi\Big|_{\tilde{x}^-} = \phi\Big|_{\tilde{x}^+},\quad h(\tilde{x}^-)\frac{d\phi}{dx}\Big|_{\tilde{x}^-} = h(\tilde{x}^+)\frac{d\phi}{dx}\Big|_{\tilde{x}^+}. \tag{40}$$

Using Equation (39) and the matching conditions as in Equation (40), we get following matrix relation in the product form as

$$\begin{pmatrix} 1 \\ A_R \end{pmatrix} = \prod_{j=2}^{N} \left(H_1^{-1} P_1 H_2^{-1} S_1 \right)^{(j-1)} (H_1^{-1} P_1 H_2^{-1}) S_2 H_3^{-1} \begin{pmatrix} p_1 \\ p_2 \end{pmatrix} D^3 = \begin{pmatrix} a_1 \\ a_2 \end{pmatrix} D^3, \quad (41)$$

where square matrices $H_1,\ H_2,\ H_3, S_1, S_2, P_1$ are defined as

$$H_1 = \begin{pmatrix} 1 & 1 \\ k_1 h_1 & -k_1 h_1 \end{pmatrix}, H_2 = \begin{pmatrix} 1 & 1 \\ k_2 h_2 & -k_2 h_2 \end{pmatrix}, H_3 = \begin{pmatrix} 1 & 1 \\ ik_1 & -ik_1 \end{pmatrix},$$

$$P_1 = \begin{pmatrix} e^{-ik_2 w} & e^{ik_2 w} \\ k_2 h_2 e^{-ik_2 w} & -k_2 h_2 e^{ik_2 w} \end{pmatrix},$$

$$S_1 = \begin{pmatrix} e^{ik_1(w-d)} & e^{-ik_1(w-d)} \\ k_1 h_1 e^{ik_1(w-d)} & -k_1 h_1 e^{-ik_1(w-d)} \end{pmatrix}, S_2 = \begin{pmatrix} e^{-ik_1 L_g} & e^{ik_1 L_g} \\ k_1 h_1 e^{-ik_1 L_g} & -k_1 h_1 e^{ik_1 L_g} \end{pmatrix},$$

with

$$p_1 = 1 + \frac{m_5 - m_3}{m_3 - m_4} \left(\frac{m_5}{m_4} \right)^4 + \frac{m_4 - m_5}{m_3 - m_4} \left(\frac{m_5}{m_3} \right)^4,$$
$$p_2 = m_5 + \frac{m_5 - m_3}{m_3 - m_4} \left(\frac{m_5}{m_4} \right)^4 m_4 + \frac{m_4 - m_5}{m_3 - m_4} \left(\frac{m_5}{m_3} \right)^4 m_3.$$

Finally, using Equation (41), the reflection coefficient is obtained as $K_r = |A_R| = |a_2/a_1|$.

Moreover, the spatial components of the free surface elevation $\eta(x)$ and the plate deflection $\nu(x)$ are obtained as

$$\eta(x) = \mathrm{Re}\left\{ \left(\frac{ih(x)}{\omega} \right) \phi_{1xx}(x) \right\}, \qquad \nu(x) = \mathrm{Re}\left\{ \left(\frac{ih_1}{\omega} \right) \phi_{2xx}(x) \right\}, \quad (42)$$

where $h(x)$ is the water-depth as defined in Equation (8).

6. Results and Discussions

In this section, using MATLAB software, numerical codes are written to analyze the effect of a semi-infinite floating plate on Bragg scattering of surface waves by multiple undulations in the seabed. Various non-dimensional physical parameters, such as width w/L_1, gap between the leading edges of two adjacent trenches/breakwaters $2d/L_1$ of trench/breakwater, gap between right-most trench/breakwater, and plate L_g/L_1, are considered for the analysis of Bragg scattering of gravity waves, as in Kar et al. [18]. Moreover, the values of different physical parameters, such as water depth $h_1 = 5$ m, incident wavelength $L_1 (= 2\pi/k_1) = 40\pi$ m, and plate rigidity $D/\rho g = 10^5$ m^4 (same as considered by Kalyanaraman et al. [12]), and mass density of the plate is $m_s = \rho_i d_i$, with density of ice $\rho_i = 922$ kg m^{-3}, plate thickness $d_i = 1$ m, density of water $\rho = 1025$ kg m^{-3}, and $g = 9.81$ ms^{-2} are kept fixed, unless stated otherwise.

6.1. Semi-Infinite Plate in the Absence of Bottom Undulation

In Figure 3, the reflection coefficient K_r is plotted against wavenumber $k_1 h_1$ for different values of (Figure 3a) rigidity $D/\rho g$ with $h_1 = 5$ m and (Figure 3b) water depth h_1 with rigidity $D/\rho g = 10^5$ m^4 in the absence of bottom bed undulation. In Table 1, the energy identity as in Equation (31) for various wave number are computed in case of waves scattering by semi-infinite floating flexible plate in finite water depth. The relative

errors corresponding to Figure 3a is provided in Table 2. It is to be noted that the relative error is calculated by comparing the BEM-based results with the analytic results. Table 2 reveals that the maximum relative error is less than 5%, which depends on the wave number k_1h_1. Figure 3a shows that, for a higher wave number, reflection increases rapidly compared to the lower wavenumber values. Figure 3a depicts that, with an increase of rigidity of ice-sheet, wave reflection coefficient K_r increases, which is similar as observed in Sahoo et al. [3]. In Figure 3b, reflection coefficient K_r decreases as water depth h_1 increases with an increases in wavenumber k_1h_1 which may be due to less resonance in higher water depth h_1. Figure 3 reveals that resonance in wave reflection does not occur as the wave number increases for the semi-infinite plate in the absence of seabed undulations. Further, Figure 3a,b reveal that rigidity of the plate has more effect on wave reflection compared to water depth. Moreover, both the sub-figures reveal that the various computational results obtained via the numerical method agree well with the analytic solution, as discussed in the case of long waves. Thus, in the subsequent study, our analyses will be based on the analytic solution associated with long waves.

Table 1. Energy identity as in Equation (31) for waves scattering by semi-infinite floating flexible plate in finite water depth case.

k_1h_1	$D/\rho g$ in m^4	BEM-Based Solution		
		K_r^2	γK_t^2	$K_r^2+\gamma K_t^2$
0.1	10^5	0.00011	0.99988	0.99999
	10^6	0.00088	0.99912	1.00000
	10^7	0.00830	0.99169	0.99999
	10^8	0.02147	0.97852	0.99999
0.2	10^5	0.00146	0.99853	0.99999
	10^6	0.00989	0.99010	0.99999
	10^7	0.02345	0.97654	0.99999
	10^8	0.05330	0.94669	0.99999
0.3	10^5	0.00615	0.99384	0.99999
	10^6	0.01784	0.98216	1.00000
	10^7	0.04025	0.95974	0.99999
	10^8	0.09604	0.90395	0.99999
0.4	10^5	0.01108	0.98891	0.99999
	10^6	0.02560	0.97439	0.99999
	10^7	0.06206	0.93793	1.00000
	10^8	0.14006	0.85993	0.99999

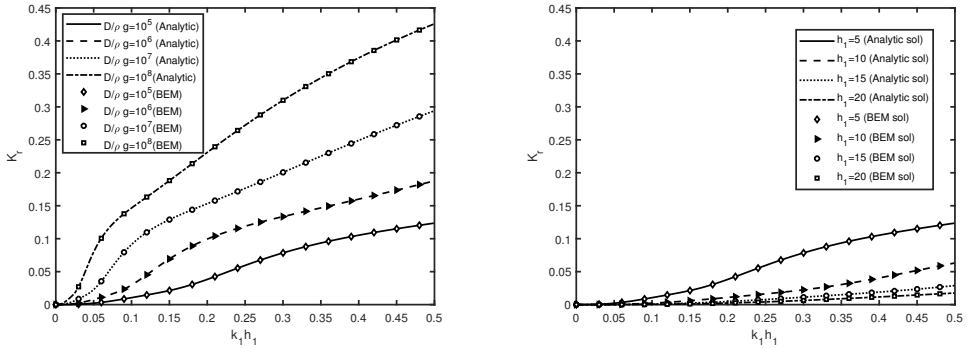

(**a**) (**b**)

Figure 3. Semi-infinite plate for different values of (**a**) rigidity $D/\rho g$ with $h_1 = 5$ m; (**b**) water depth h_1 with $D/\rho g = 10^5$ m^4 in the absence of trenches/breakwaters.

Table 2. Relative error corresponding to Figure 3a.

k_1h_1	$D/\rho g$	Analytic Solution	BEM-Based Solution	Relative Error
0.1	10^5	0.01056	0.01102	0.04356
	10^6	0.02972	0.02851	0.04071
	10^7	0.09113	0.09254	0.01547
	10^8	0.14655	0.14962	0.02094
0.2	10^5	0.03826	0.03751	0.01960
	10^6	0.09944	0.09786	0.01588
	10^7	0.15316	0.15759	0.02892
	10^8	0.23088	0.23147	0.00255
0.3	10^5	0.07847	0.07954	0.01363
	10^6	0.13355	0.13627	0.02036
	10^7	0.20064	0.20283	0.01091
	10^8	0.30990	0.31006	0.00051
0.4	10^5	0.10529	0.10725	0.01861
	10^6	0.16001	0.16230	0.01431
	10^7	0.24912	0.25013	0.00405
	10^8	0.37425	0.37870	0.01189
0.5	10^5	0.12367	0.12427	0.00485
	10^6	0.18771	0.18927	0.00831
	10^7	0.29405	0.29514	0.00370
	10^8	0.42597	0.42647	0.00117

6.2. Trenches/Breakwaters in the Absence of Semi-Infinite Plate

The reflection coefficient K_r versus trench width w/L_1 is plotted in Figure 4 for different number N of rectangular (a) trenches and (b) breakwaters in the absence of semi-infinite plate with gap $d/L_1 = 0.6$, $L_1 = 40\pi$ m. Figure 4a depicts the occurrence of common zero minima in wave reflection irrespective of the number of trenches when w/L_1 is an integer multiple of 0.6 and alternately maxima occur between two consecutive zero minima in wave reflection. On the other hand, Figure 4b reveals that, in case of breakwaters, zeros in reflection occur when w/L_1 is an integer multiple of 0.35, whilst maxima in wave reflection occurs between consecutive minima. Further, both the sub-figures depict that the reflection coefficient increases as the number of submerged trenches/breakwaters increases. A comparison of both the sub-figures reveals that optima in wave reflection occur for smaller values of w/λ in case of submerged breakwaters than that of the submerged trenches. Further, for the same number of trenches/breakwaters, it may be noted that the maximum amplitude of wave reflection is smaller in the case of submerged trenches than that of the breakwaters. Further, both the sub-figures depict that Bragg reflection occurs in the presence of multiple submerged trenches and breakwaters. Moreover, occurrence of sub-harmonic peaks are noticed when the number of trenches/breakwaters are more than two, which is similar to the observation made in Kar et al. [29,30]. In the subsequent analyses, the values of $w/L_1 = 0.6$ in case of submerged trenches and $w/L_1 = 0.35$ in case of breakwaters are kept fixed, unless otherwise mentioned.

In Figure 5, reflection coefficient K_r is plotted against gap $2d/L_1$ for different number N of rectangular (Figure 5a) trenches with width $w/L_1 = 0.6$ and (Figure 5b) breakwaters with width $w/L_1 = 0.35$ in the absence of semi-infinite plate with $L_1 = 40\pi$ m. Figure 5a shows that all the curves attain their minima for $2d/L_1 = 0.72,\ 1.72,\ 2.71$ in the case of trenches, whereas, in Figure 5b, all curves attain their minima for $2d/L_1 = 0.21,\ 1.21,\ 2.21$. Therefore, both the figures reveal that, in the case of an even number of trenches or breakwaters, all the curves match if the gap in between the adjacent sides of trenches or breakwaters is half of the wavelength of the incident wave, i.e., $d = n\frac{L_1}{2},\ n \in \mathbb{Z}_+$. Hence, we keep fix the values of $d/L_1 = 0.86$ in case of trenches, whereas $d/L_1 = 0.60$ in case of breakwaters for which minima in wave reflection occur in case of even and odd number of

trenches or breakwaters. Further, it may be noted that, between two harmonic peaks, $N-2$ sub-harmonic peaks occur, with N being the number of submerged trenches/breakwaters with Bragg reflection occurring in the presence of multiple undulations irrespective of submerged trenches or breakwaters. A similar observation has been noticed in Figure 4.

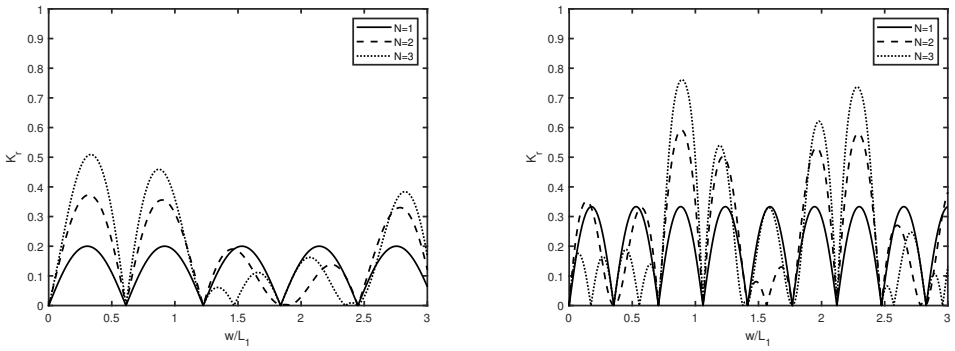

Figure 4. Reflection coefficient K_r versus width w/L_1 for different number N of rectangular (**a**) trenches; (**b**) breakwaters in the absence of semi-infinite ice sheet with gap $d/L_1 = 0.6$, $L_1 = 40\pi$ m.

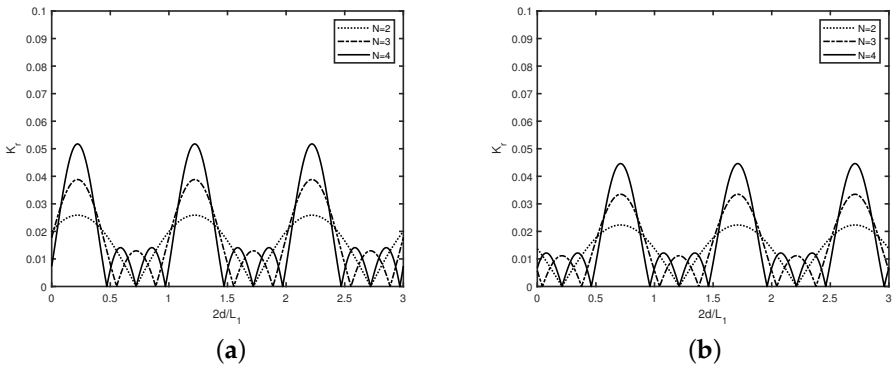

Figure 5. K_r versus gap $2d/L_1$ for different number N of rectangular (**a**) trenches with width $w/L_1 = 0.6$; (**b**) breakwaters with width $w/L_1 = 0.35$ in the absence of the semi-infinite plate with $L_1 = 40\pi$ m.

In Figure 6, the variation of the reflection coefficient K_r versus wave number k_1h_1 is shown for a single rectangular submerged (Figure 6a) trench and (Figure 6b) breakwater in the absence of semi-infinite plate for different widths w/L_1, as mentioned in Table 3. It is observed that a complete cycle occur when wave number $k_1h_1 = 0.25n$, $n \in \mathbb{Z}_+$ irrespective of single trench or breakwater (see Table 4). Further, common maxima/minima occur in wave reflection in case of trenches and breakwaters within periodic range of the values of k_1h_1. Similar results has been observed in Figures 4 and 5 with variation of gap, as well as width of trenches/breakwaters, and also in Reference [18]. Moreover, Figure 6a,b reveal that the amplitude of the peaks are constant irrespective of the width w/L_1 for a single trench/breakwater.

In Figure 7, the variation of reflection coefficient K_r versus wave number k_1h_1 is exhibited in case of double rectangular (Figure 7a) trenches with width $w/L_1 = 0.6$ and (Figure 7b) breakwaters with $w/L_1 = 0.35$ for different values of $2d/L_1$ in the absence of semi-infinite plate. Figure 7a,b reveal that cycles are completed at the same values of wave number k_1h_1. Moreover, amplitude of peak in the reflection coefficient K_r remains constant for different values of $2d/L_1$ in case of both of trenches and breakwaters. Further, Figure 7 reveals that, with an increase in gap $2d/L_1$, amplitude of harmonic peak in wave reflection

increases in each cycle with an increase in wave number k_1h_1. Further, it may be noted that sub-harmonic peak does not occur as reflection coefficient K_r is plotted in case of double trenches and breakwaters.

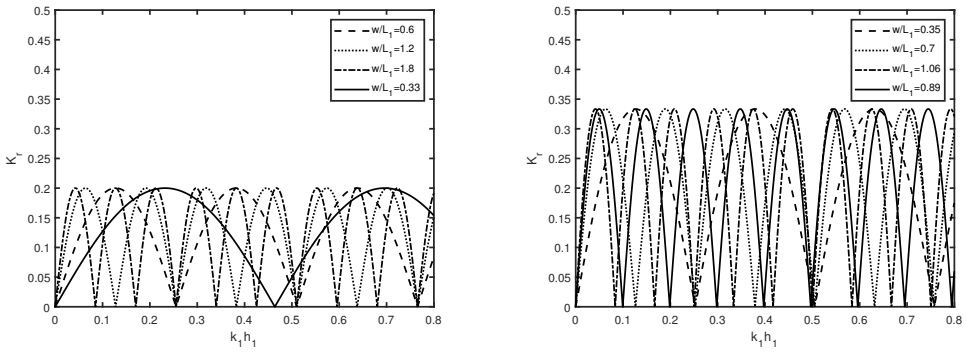

(**a**) (**b**)

Figure 6. K_r versus wave number k_1h_1 in case of single rectangular (**a**) trench; (**b**) breakwater in the absence of semi-infinite plate with different widths w/L_1, $L_1 = 40\pi$ m.

Table 3. Values of w/L_1, $2d/L_1$ for common min/ max of K_r in case N number of trenches/breakwaters.

		$\min\{K_r\}$			$\max\{K_r\}$
Trenches	w/L_1	0.6	1.2	1.8	0.33
Trenches	$2d/L_1$	0.72	1.72	2.73	1.22
Breakwaters	w/L_1	0.35	0.70	1.06	0.89
Breakwaters	$2d/L_1$	0.20	1.20	2.20	1.71

Table 4. Values of k_1h_1 for common minimum of reflection coefficient for different values of w/L_1.

		$\min\{K_r\}$		
Single trench	k_1h_1	0.25	0.51	0.76
Single breakwater	k_1h_1	0.25	0.50	0.75

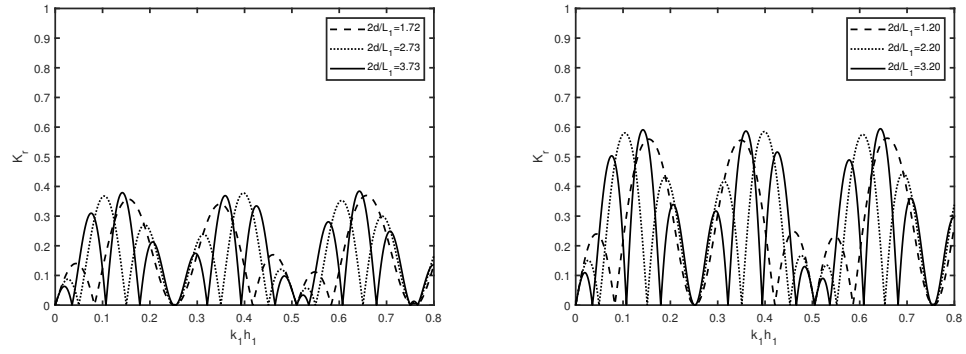

(**a**) (**b**)

Figure 7. K_r versus k_1h_1 in case of double rectangular (**a**) trench width $w/L_1 = 0.6$; (**b**) breakwater with width $w/L_1 = 0.35$ in the absence of the semi-infinite plate for different values of gaps $2d/L_1$.

In Figure 8, the reflection coefficient K_r is plotted against wavenumber k_1h_1 for different number N of rectangular (Figure 8a) trenches with width $w/L_1 = 0.6$, $d/L_1 = 0.86$ and (Figure 8b) breakwaters with $w/L_1 = 0.35$, $d/L_1 = 0.60$ in the absence of semi-infinite plate. Figure 8a reveals that three full cycles are completed in case of trenches at $k_1h_1 = 0.25,\ 0.5,\ 0.75$, whereas, in Figure 8b, in case of breakwaters, three full cycles are

completed for the same wavenumber in the range $0 < k_1h_1 < 0.8$ with an increase in N for different values of trenches and breakwaters widths and gap as mentioned in Table 3. Figure 8a,c describes the comparison between the trenches and breakwaters. It is observed that the number of full cycles in the case of trenches is two less than that of breakwaters. This happens due to the formation of nodes or anti-nodes along the interface boundaries of the trenches and breakwaters. Moreover, the number of common zero minima in the case of breakwaters is two greater than that of trenches. Further, the amplitude of the harmonic peaks, i.e., peaks in each bandwidth are not equal as the number of trenches or breakwaters increases. As the number of trenches or breakwaters N increases, the sub-harmonic peaks occur, which is similar to that of the phenomena observed in Kar et al. [29] in the case of scattering of gravity waves by an array of trenches.

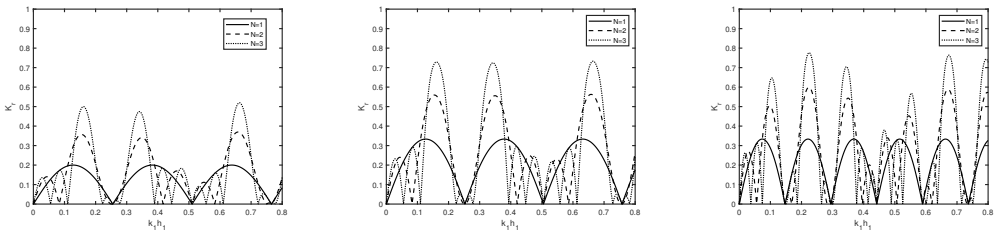

(**a**) (**b**) (**c**)

Figure 8. Reflection coefficient K_r versus wave number k_1h_1 for different number N of rectangular trenches with (**a**) width $w/L_1 = 0.6$, gap $d/L_1 = 0.86$, and breakwaters with (**b**) width $w/L_1 = 0.35$, gap $d/L_1 = 0.60$ and (**c**) width $w/L_1 = 0.6$, gap $d/L_1 = 0.86$ in the absence of the semi-infinite plate.

In Figure 9, the reflection coefficient K_r is plotted against wave number k_1h_1 for different depths h_2/h_1 of (Figure 9a) submerged trenches with $w/L_1 = 0.6$, $d/L_1 = 0.86$ and (Figure 9b) breakwaters with $w/L_1 = 0.35$, $d/L_1 = 0.6$ in the absence of semi-infinite plate with $N = 2$. Figure 9a reveals that, with an increase in trench depth, the reflection coefficient increases with a rise in wave number. Figure 9b reveals that, as breakwater height decreases, wave reflection coefficient K_r decreases with an increase in wave number k_1h_1, which occurs as more wave energy is trapped due to higher values of breakwaters height. From Figure 9a,b, it is observed that, for a smaller wave number, phase-shift of the wave reflection matches, whereas, for a higher wave number, it does not occur.

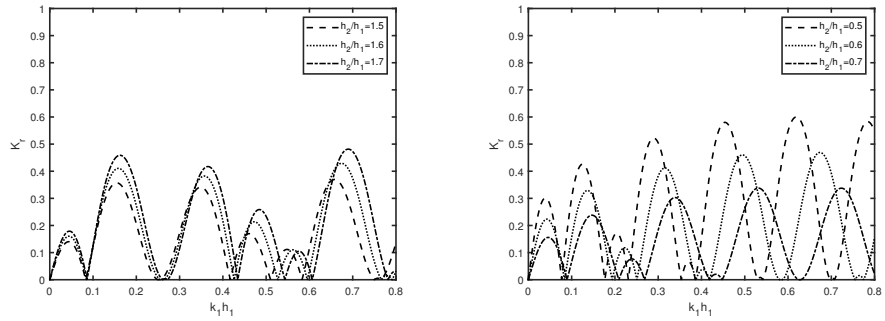

(**a**) (**b**)

Figure 9. K_r versus k_1h_1 in case of different depth h_2/h_1 of double rectangular (**a**) trenches with $w/L_1 = 0.6$, $d/L_1 = 0.86$; (**b**) breakwaters with $w/L_1 = 0.35$, $d/L_1 = 0.6$ in the absence of a semi-infinite plate.

6.3. Plate-Trench Combination

In Figure 10, the variation of the reflection coefficient K_r versus wavenumber k_1h_1 is demonstrated for different values of single (Figure 10a) trench and (Figure 10b) breakwater width w/L_1 (as mentioned in Table 3) with plate rigidity $D/\rho g = 10^5 \mathrm{m}^4$ in the presence of semi-infinite plate. Figure 10a reveals that results obtained by both analytic and numerical

methods agree well in the presence of a single trench and a semi-infinite plate. Figure 10a depicts that number of complete cycles are fixed, as observed in Figure 6a. However, because of the presence of floating plate, wave reflection increases, in general, irrespective of the values of the wavenumber k_1h_1, and zero minima in wave reflection does not occur for higher values of wave number, which is due to the partial reflection of surface waves with an increase in wavenumber, as observed in Figure 3. The notation '$\circ$' denotes the points where minima in wave reflection occur exactly for the same wave number except for certain non-zero values of the reflection coefficient. Further, Figure 10b reveals that the number of common minima in wave reflection remains the same as observed in Figure 6b in the absence of floating plate. Similar phenomena is observed in the case of Bragg reflection of surface gravity waves by an array of rectangular breakwaters in the presence of a floating dock, as in Kar et al. [30]. Figure 10a,b reveals that the number of bandwidth remain constant irrespective of the increase in the width of the trench/breakwater w/L_1. However, the number of oscillations in each cycle/bandwidth increases apart from an increase in the value of minima in wave reflection, which is due to the presence of the floating elastic plate.

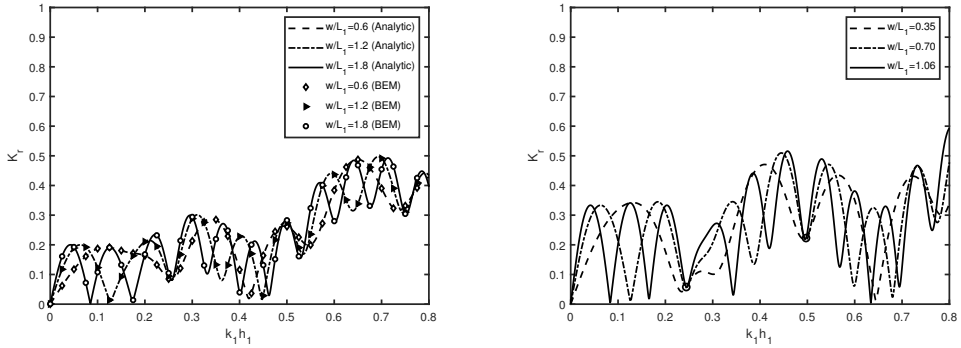

(**a**) (**b**)

Figure 10. Reflection coefficient K_r versus wave number k_1h_1 in case of single (**a**) trench and (**b**) breakwater in the presence of the semi-infinite plate for different values of w/L_1 with $L_g/L_1 = 0.25$ and $D/\rho g = 10^5$ m^4.

In Figure 11, the variation of the reflection coefficient K_r versus wave number k_1h_1 is exhibited for different number N of trenches in Figure 11a,b with $w/L_1 = 0.6$ and $d/L_1 = 0.86$, and breakwaters in Figure 11c,d with $w/L_1 = 0.35$ and $d/L_1 = 0.6$ in the presence of the semi-infinite plate with $L_g/L_1 = 0.25$ and $D/\rho g = 10^5$ m^4. Figure 11 reveals that, with an increase in the number N of trenches and breakwaters, the amplitude of peak in the band-width increases, whereas the length of the band-width decreases. The decrease in bandwidth is due to an increase in the resonating interaction within the gap between the trenches and breakwater, whilst the increase in the amplitude of the resonating peaks is due to the superposition of the higher number of standing waves generated within the trenches/breakwaters and the gaps between them. Further, it is observed that, irrespective of trenches and breakwaters, for a certain wave-number, common minimum occurs when N is even, whereas maximum occurs at 180^o out of phase when N is odd. A similar observation has been found in the absence of the semi-infinite plate in Kar et al. [18], except the rise in the minima in wave reflection in the presence of the plate. However, Bragg reflection occurs in both the cases of multiple trenches and breakwaters in isolation in the presence of the semi-infinite plate. Moreover, at $k_1h_1 = 0.5$, one cycle is completed in the case of breakwaters, whereas, in the case of trenches, one sub-harmonic peak is observed, which is similar to Figure 10. A comparison among the Figures 6, 8, 10, and 11 depicts that, in the presence of semi-infinite plate, the position of cycle shifts upward, as observed in the absence of semi-infinite plate.

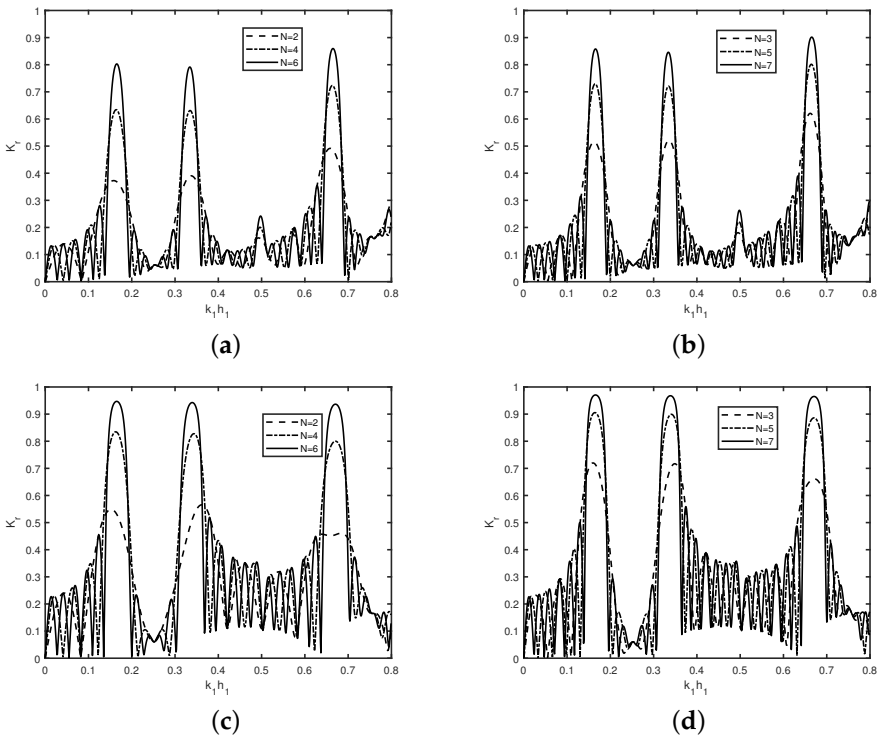

Figure 11. K_r versus k_1h_1 for different number N of (**a**,**b**) trenches with $w/L_1 = 0.6$, $d/L_1 = 0.86$; (**c**,**d**) breakwaters with $w/L_1 = 0.35$, $d/L_1 = 0.6$, in the presence of a semi-infinite plate with $L_g/L_1 = 0.25$, $D/\rho g = 10^5$ m^4.

In Figure 12, the reflection coefficient K_r is plotted against the wavenumber k_1h_1 for different values of depth ratios h_2/h_1 of (Figure 12a) trenches with $w/L_1 = 0.6$ $d/L_1 = 0.86$, and (Figure 12b) breakwaters with $w/L_1 = 0.35$, $d/L_1 = 0.6$ in the presence of a semi-infinite plate. Figure 12 reveals that the reflection coefficient K_r increases, in general, with an increase in depth ratio h_2/h_1 in case of multiple trenches, whilst wave reflection decreases in the case of breakwaters, which is similar as observed in Figure 9. Further, zero reflection does not occur in the presence of a semi-infinite plate. Further, it is observed that higher wave reflection occur with an increase k_1h_1, which is due to the combined effect of Bragg reflection due to multiple bottom undulations and the wave reflection by the semi-infinite plate, which is clear from Figures 3 and 9. Moreover, optima in wave reflection occur for smaller values of wavenumber with an increase in depth of the trench and the height of the breakwater due to the variation in the wavelength of the standing waves generated over the trench/breakwater.

In Figure 13, the reflection coefficient K_r is plotted against the wavenumber k_1h_1 for different values of rigidity $D/\rho g$ in case of (Figure 13a) trenches with $w/L_1 = 0.6$, $d/L_1 = 0.86$ (Figure 13b) breakwaters with $w/L_1 = 0.35$, $d/L_1 = 0.6$ in the presence of semi-infinite plate with $L_g/L_1 = 0.25$ and $N = 3$. It is observed that the wave reflection increases as in oscillatory for higher values of wave number with an increase in the structural rigidity $D/\rho g$, which is due to the reflection of the higher amount of wave energy by the semi-infinite plate, as observed in Figure 3a. However, the number of oscillation remains the same as the number of submerged trenches/breakwaters remain unchanged. As the rigidity of the plate $D/\rho g$ increases, the wave reflection increases, which is similar as observed in Figure 3a. Moreover, the number of oscillations in wave reflection remains unchanged with an increase in rigidity $D/\rho g$, which is due to the presence of the same no of trenches/breakwaters.

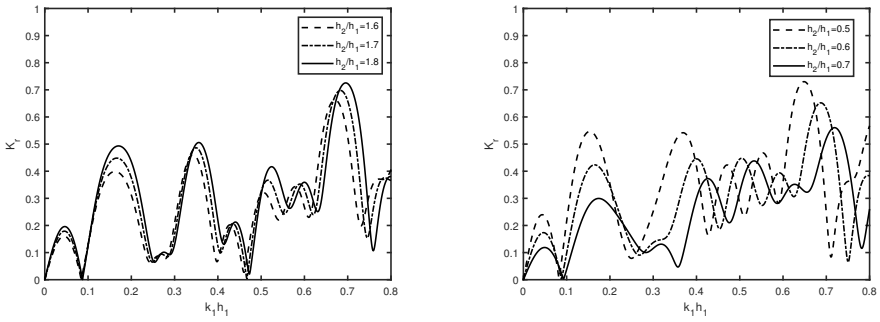

(**a**) (**b**)

Figure 12. K_r versus k_1h_1 in case of different depth h_2/h_1 of double (**a**) rectangular trenches with $w/L_1 = 0.6$, $d/L_1 = 0.86$; (**b**) breakwaters with $w/L_1 = 0.35$, $d/L_1 = 0.6$ in the presence of a semi-infinite plate.

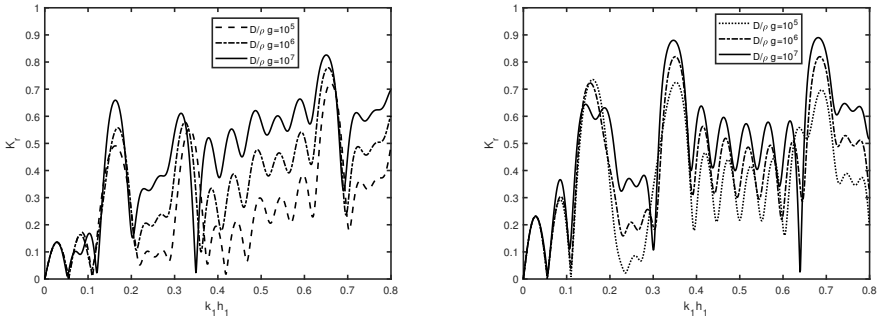

(**a**) (**b**)

Figure 13. K_r versus k_1h_1 for different values of rigidity $D/\rho g$ in the case of (**a**) trenches with $w/L_1 = 0.6$, $d/L_1 = 0.86$; (**b**) breakwaters with $w/L_1 = 0.35$, $d/L_1 = 0.6$ in the presence of a semi-infinite plate with $L_g/L_1 = 0.25$ and $N = 3$.

In Figure 14, the variation of reflection coefficient K_r versus gap width $2d/L_1$ is demonstrated for different number of (Figure 14a) submerged trenches with $w/L_1 = 0.33$ and (Figure 14b) breakwaters with $w/L_1 = 0.89$ in the presence of the semi-infinite plate with $D/\rho g = 10^5$ m^4 and $L_g/L_1 = 0.25$. Figure 14 demonstrates that the reflection coefficient K_r is periodically oscillatory in nature with an increase in the gap width $2d/L_1$, which is similar to that of Figure 5. However, wave reflection increases, in general, with an increase in the gap width in the presence of the semi-infinite plate. A comparison of Figure 14a,b reveals that both the sub-figures have the same number of harmonic peaks, whereas the bandwidth of each harmonic peaks shifts forward in the case of breakwaters than that of trenches, which is due to the change of phase of the seabed profiles from trenches to that of breakwaters.

Figure 15 exhibits the variation of the reflection coefficient K_r versus the gap between the semi-infinite plate and the adjacent submerged trench/breakwater L_g/L_1 for different number N of (Figure 15a) trenches with $w/L_1 = 0.33$, $d/L_1 = 0.61$, and (Figure 15b) breakwaters with $w/L_1 = 0.89$, $d/L_1 = 1.37$ in the presence of the semi-infinite plate with $D/\rho g = 10^5$ m^4. Figure 15 reveals that irrespective of No. of trenches/breakwaters, periodic oscillatory patterns in the wave reflection is observed. Further, with an increase in number of trenches/breakwaters N, amplitude of reflection increases. Moreover, the reflection pattern in the case of submerged trenches is 180° out of phase to that of breakwaters, which is similar to that of Figure 11c,d.

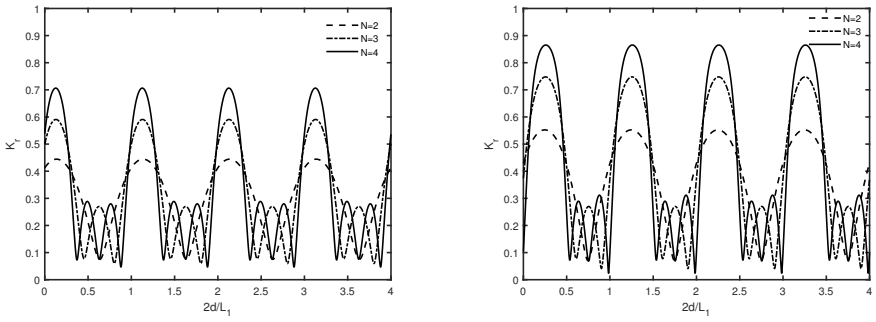

(**a**) (**b**)

Figure 14. Reflection coefficient K_r versus gap $2d/L_1$ for different number of (**a**) trenches with $w/L_1 = 0.33$; (**b**) breakwaters with $w/L_1 = 0.89$ in the presence of a semi-infinite plate with $D/\rho g = 10^5$ m^4, $L_g/L_1 = 0.25$.

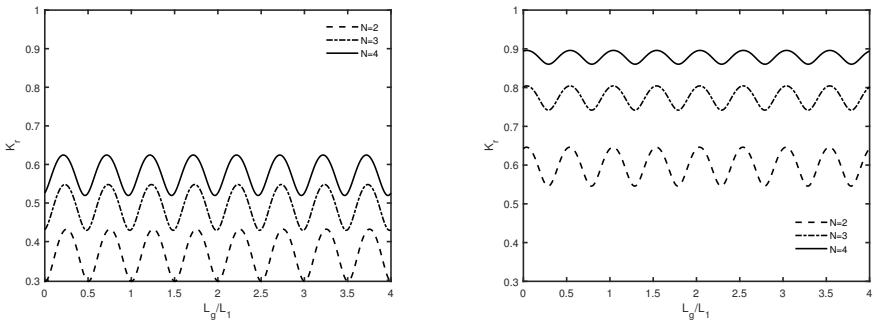

(**a**) (**b**)

Figure 15. Reflection coefficient K_r versus gap L_g/L_1 in case of different number N of trenches with (**a**) $w/L_1 = 0.33$, $d/L_1 = 0.61$, and breakwaters with (**b**) $w/L_1 = 0.89$, $d/L_1 = 1.37$ in the presence of the semi-infinite plate with $D/\rho g = 10^5$ m^4.

7. Time Dependent Displacement

Using Equation (42), the free surface displacement $\zeta_c(x,t)$, as a combination of the free surface elevation $\zeta(x,t)$ and the flexible plate deflection $\tau(x,t)$, is obtained as

$$\zeta_c(x,t) = \begin{cases} \zeta(x,t), & x < p, \\ \tau(x,t), & x > p, \end{cases} \tag{43}$$

where $\tau(x,t)$ and and $\zeta(x,t)$ are computed using the formulae

$$\zeta(x,t) = \mathrm{Re}\left\{ \int_{-\infty}^{\infty} \tilde{f}(\omega)\zeta(x,\omega)e^{-i\omega t}d\omega \right\}, \tag{44}$$

$$\tau(x,t) = \mathrm{Re}\left\{ \int_{-\infty}^{\infty} \tilde{f}(\omega)\tau(x,\omega)e^{-i\omega t}d\omega \right\}, \tag{45}$$

with $\tilde{f}(\omega)$ being the Fourier transform of the incident wave pulse. In Equations (44) and (45), $\zeta(x,\omega)$ and $\tau(x,\omega)$ are the frequency dependent surface displacement of the open water and the semi-infinite plate covered region, respectively. Assume the incident wave pulse as a Gaussian wave packet which is of the form $\tilde{f}(\omega) = \sqrt{\frac{b}{\pi}}e^{-b(\omega-\omega_0)^2}$, with b being the spreading function, and ω_0 being the central frequency of the incident wave pulse.

In Figures 16–20, the free surface displacement $\zeta_c(x,t)$ is plotted as a function of space x and time t for a semi-infinite plate with flat bed, in the presence of single and double trenches, as well as in the presence of single and double breakwaters, respectively.

All the figures reveal that Bragg scattering of the wave pulses that occurs at each boundary of trench/breakwater and at one edge of the semi-infinite plate, which is similar to the observation made in Kar et al. [18]. It is observed that wave energy vanishes for extended times irrespective of the presence of the trench or breakwater. Moreover, it is observed that, in the case of multiple undulations, the resonance of wave pulse becomes higher as compared to that of single undulation.

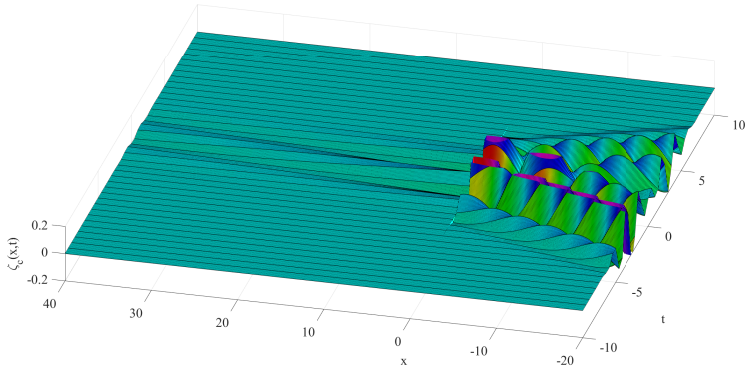

Figure 16. Variation of the free surface displacement $\zeta_c(x,t)$ (m) versus x (m) and time t (s) in the case of a semi infinite plate in the case of flat seabed.

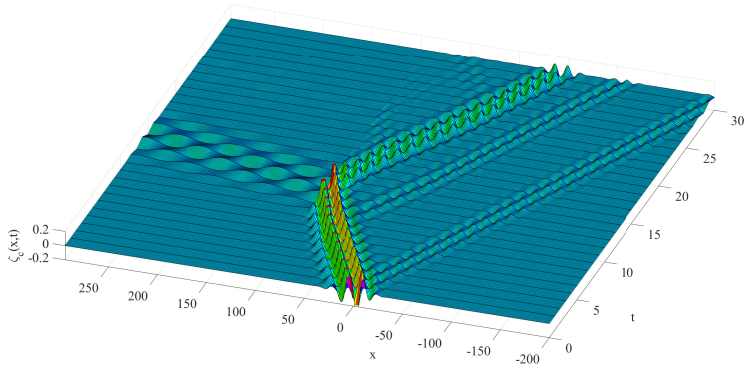

Figure 17. Variation of the free surface displacement $\zeta_c(x,t)$ (m) versus x (m) and time t (s) in the case of a semi-infinite plate in the presence of a single trench.

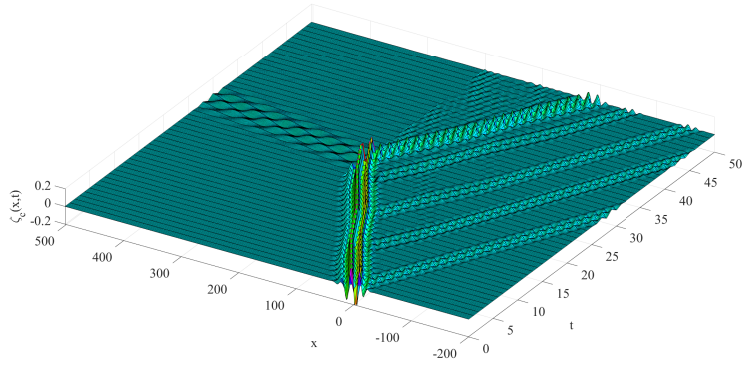

Figure 18. Variation of the free surface displacement $\zeta_c(x,t)$ (m) versus x (m) and time t (s) in the case of a semi-infinite plate in the presence of double trenches.

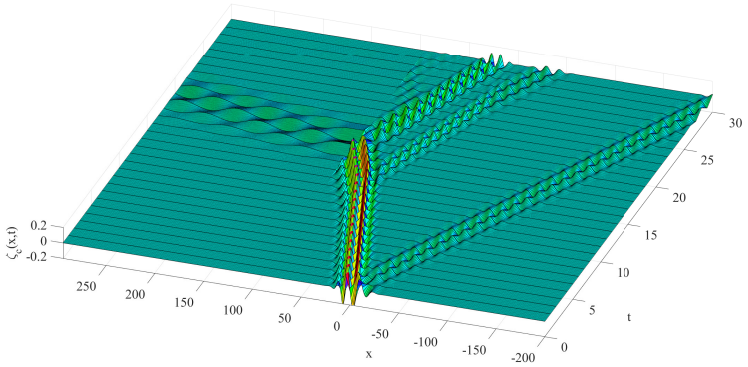

Figure 19. Variation of the free surface displacement $\zeta_c(x,t)$ (m) versus x (m) and time t (s) in the case of a semi-infinite plate in the presence of single breakwater.

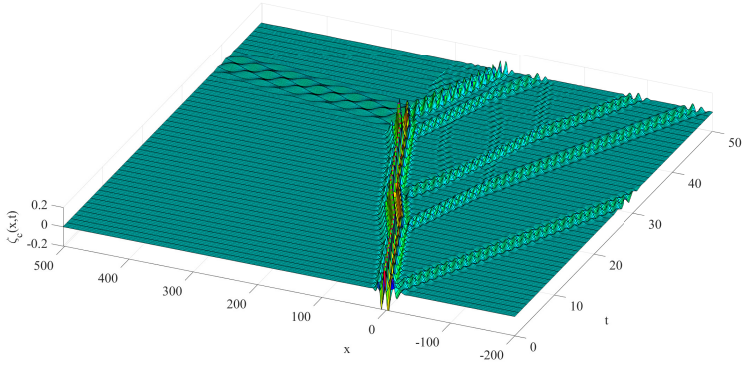

Figure 20. Variation of the free surface displacement $\zeta_c(x,t)$ (m) versus x (m) and time t (s) in the case of a semi-infinite plate in the presence of double breakwaters.

8. Conclusions

In the present study, Bragg scattering by multiple submerged trenches/breakwaters in isolation has been studied in the presence of a semi-infinite plate under the assumption of linear small amplitude water wave theory, as well as structural response in finite water depth, using BEM. Further, the closed-form analytical solution is obtained under the premise of linear long wave theory by matching the continuity of pressure and mass flux at the interface boundaries. Results obtained through the BEM approach are validated using energy identity and compared with the analytic solutions based on shallow water approximation. Further, the present study reveals that Bragg resonance of long waves occurs due to the presence of an array of trenches or breakwaters, along with a semi-infinite floating plate apart from the array of trenches or breakwaters in isolation. The amplitude of oscillation in the reflection coefficient K_r increases as the rigidity of the plate $D/\rho g$ increases. Further, both peak amplitude and band-width in Bragg reflection increase in the case of an array of submerged breakwaters compared to trenches. The pattern of wave reflection is a periodically oscillatory function of the gap between trenches and the semi-infinite plate. The free surface displacement is plotted in the presence of the seabed undulations and the semi-infinite plate using time-series analysis. The study will help to understand wave transformation in the marginal ice zone and in the design of very large floating structures in the presence of bottom undulation. Moreover, the study can have potential application in the extraction of wave energy and creation of the tranquility zone in marine environment. The current work can be extended to study the effect of lateral compression and variable thickness of the semi infinite plate on Bragg scattering of surface wave due to undulated seabed.

Author Contributions: Conceptualization, T.S.; methodology, P.K., S.K. and K.T.; software, P.K. and S.K.; validation, P.K. and S.K.; formal analysis, P.K. and T.S.; investigation, P.K. and S.K.; resources, S.K.; data curation, P.K., S.K. and K.T.; writing—original draft preparation, P.K. and S.K.; writing—review and editing, P.K., S.K., K.T. and T.S.; visualization, P.K., S.K., K.T. and T.S.; supervision, T.S.; project administration, T.S.; funding acquisition, T.S. and S.K. All authors have read and agreed to the published version of the manuscript.

Funding: T.S. acknowledges the financial support of the Department of Science and Technology, Government of India vide award No. DST/CCP/CoE/79/2017(G). P.K. gives thanks to Medinipur College, West Bengal, for financial support vide award No. 334/2/MC/RUSA 2.0/ASST. PROF/APPT/2021. S.K. and K.T. acknowledge the financial support received through the DST Project: DST/INSPIRE/04/2017/002460 to pursue this research work.

Institutional Review Board Statement: Not applicable.

Informed Consent Statement: Not applicable.

Data Availability Statement: The data that support the findings of this study are available from the corresponding author upon reasonable request.

Acknowledgments: P.K. is grateful to M. H. Meylan of The University of Newcastle, Australia, for introducing him to the time domain simulation during his visit to IIT Kharagpur in December 2019.

Conflicts of Interest: The authors declare no conflict of interest.

Appendix A

The boundary of the computational domain, as exhibited in Figure 2, is divided into finite number of boundary elements. Assuming ϕ and $\partial\phi/\partial n$ are linearly varying over each element, the integral equation in Equation (23) is converted into a system of linear equations as given by

$$\sum_{j=1}^{N_l}\left(H^{ij}-\mathrm{i}k_1G^{ij}\right)\phi_j\Big|_{\Gamma_l}+\sum_{j=1}^{N_p}\left(\phi_jH^{ij}-G^{ij}\mathcal{G}(\phi_j)\right)\Big|_{\Gamma_p}+\sum_{j=1}^{N_r}\left(H^{ij}-\mathrm{i}p_1G^{ij}\right)\phi_j\Big|_{\Gamma_r}$$
$$+\sum_{j=1}^{N_b}\left(H^{ij}\right)\phi_j\Big|_{\Gamma_b}+\sum_{j=1}^{N_f}\left(H^{ij}+KG^{ij}\right)\phi_j\Big|_{\Gamma_f}=\sum_{j=1}^{N_l}\left(\frac{\partial\phi_j^I}{\partial n}-\mathrm{i}k_1\phi^I\right)G^{ij}\Big|_{\Gamma_l},$$

where $H^{ij}=C_i\delta_{ij}+\hat{H}^{ij}$, with

$$\hat{H}^{ij}=\begin{cases}h_1^{i1}+h_2^{iN} & \text{for } j=1\\ h_1^{ij}+h_2^{i,j-1} & \text{for } j=2\cdots N\end{cases},\quad G^{ij}=\begin{cases}g_1^{i1}+g_2^{iN} & \text{for } j=1\\ g_1^{ij}+g_2^{i,j-1} & \text{for } j=2\cdots N\end{cases},$$

are termed as the influence coefficients. Here, $C_i=-\alpha_i/2\pi$ with α_i being the angle between the boundary elements Γ_i and Γ_{i-1}. Further, N_J represents the total number of boundary elements over the boundary Γ_J for $J\in\{l,b,r,p,f\}$. Moreover, in the above equation, the expressions for g_k^{ij} and h_k^{ij} for $k=1,2$ are given by

$$g_1^{ij}=\frac{l_j}{4}\int_{-1}^{1}G(x(\xi),y(\xi);x_i,y_i)(1-\xi)d\xi,$$
$$g_2^{ij}=\frac{l_j}{4}\int_{-1}^{1}G(x(\xi),y(\xi);x_i,y_i)(1+\xi)d\xi,$$
$$h_1^{ij}=\frac{l_j}{4}\int_{-1}^{1}\frac{\partial G}{\partial n}(x(\xi),y(\xi);x_i,y_i)(1-\xi)d\xi,$$
$$h_2^{ij}=\frac{l_j}{4}\int_{-1}^{1}\frac{\partial G}{\partial n}(x(\xi),y(\xi);x_i,y_i)(1+\xi)d\xi,$$

with l_j being the length of the boundary element Γ_j.

References

1. Wang, C.M.; Tay, Z.Y.; Takagi, K.; Utsunomiya, T. Literature review of methods for mitigating hydroelastic response of VLFS under wave action. *Appl. Mech. Rev.* **2010**, *63*, 030802. [CrossRef]
2. Meylan, M.H.; Squire, V.A. Finite-floe wave reflection and transmission coefficients from a semi-infinite model. *Int. J. Offshore Polar Eng.* **1993**, *98*, 12537–12542. [CrossRef]
3. Sahoo, T.; Yip, T.L.; Chwang, A.T. Scattering of surface waves by a semi-infinite floating elastic plate. *Phys. Fluids* **2001**, *13*, 3215–3222. [CrossRef]
4. Squire, V.A. Synergies between VLFS hydroelasticity and sea-ice research. *Int. J. Offshore Polar Eng.* **2008**, *18*, 241–253.
5. Sturova, I.V. Time-dependent response of a heterogeneous elastic plate floating on shallow water of variable depth. *J. Fluid Mech.* **2009**, *637*, 305. [CrossRef]
6. Bhattacharjee, J.; Soares, C.G. Flexural gravity wave over a floating ice sheet near a vertical wall. *J. Eng. Math.* **2012**, *75*, 29–48. [CrossRef]
7. Papathanasiou, T.K.; Karperaki, A.E.; Theotokoglou, E.E.; Belibassakis, K.A. Hydroelastic analysis of ice shelves under long wave excitation. *Nat. Hazards Earth Syst. Sci.* **2015**, *15*, 1851–1857. [CrossRef]
8. Sturova, I.V. Motion of an external load over a semi-infinite ice sheet in the subcritical regime. *Fluid Dyn.* **2018**, *53*, 49–58. [CrossRef]
9. Das, S.; Kar, P.; Sahoo, T.; Meylan, M.H. Flexural-gravity wave motion in the presence of shear current: Wave blocking and negative energy waves. *Phys. Fluids* **2018**, *30*, 106606. [CrossRef]
10. Barman, S.C.; Das, S.; Sahoo, T.; Meylan, M.H. Scattering of flexural-gravity waves by a crack in a floating ice sheet due to mode conversion during blocking. *J. Fluid Mech.* **2021**, *916*, A11. [CrossRef]
11. Jiang, D.; Tan, K.H.; Wang, C.M.; Ong, K.C.G.; Bra, H.; Jin, J.; Kim, M.O. Analysis and design of floating prestressed concrete structures in shallow waters. *Mar. Struct.* **2018**, *59*, 301–320. [CrossRef]
12. Kalyanaraman, B.; Bennetts, L.G.; Lamichhane, B.; Meylan, M.H. On the shallow-water limit for modelling ocean-wave induced ice-shelf vibrations. *Wave Motion* **2019**, *90*, 1–16. [CrossRef]
13. Ni, B.Y.; Han, D.F.; Di, S.C.; Xue, Y.Z. On the development of ice-water-structure interaction. *J. Hydrodynam.* **2020**, *32*, 629–652. [CrossRef]
14. Belibassakis, K.A.; Athanassoulis, G.A. A coupled-mode model for the hydroelastic analysis of large floating bodies over variable bathymetry regions. *J. Fluid Mech.* **2005**, *531*, 221. [CrossRef]
15. Karmakar, D.; Bhattacharjee, J.; Sahoo, T. Oblique flexural gravity-wave scattering due to changes in bottom topography. *J. Eng. Math.* **2010**, *66*, 325–341. [CrossRef]
16. Karperaki, A.E.; Belibassakis, K.A.; Papathanasiou, T.K. Time-domain, shallow-water hydroelastic analysis of VLFS elastically connected to the seabed. *Nat. Mar. Struct.* **2016**, *15*, 33–51. [CrossRef]
17. Kar, P.; Koley, S.; Sahoo, T. Bragg scattering of long waves by an array of trenches. *Ocean Eng.* **2020**, *198*, 107004. [CrossRef]
18. Kar, P.; Sahoo, T.; Meylan, M.H. Bragg scattering of long waves by an array of floating flexible plates in the presence of multiple submerged trenches. *Phys. Fluids* **2020**, *32*, 096603. [CrossRef]
19. Koley, S. Water wave scattering by floating flexible porous plate over variable bathymetry regions. *Ocean Eng.* **2020**, *214*, 107686. [CrossRef]
20. Vijay, K.G.; Sahoo, T.; Datta, R. Wave-induced responses of a floating structure near a wall in the presence of permeable plates. *Coast. Eng. J.* **2020**, *62*, 35–52. [CrossRef]
21. Mohapatra, A.K.; Vijay, K.G.; Sahoo, T. Bragg scattering of surface gravity waves by a submerged wavy porous plate. *Ocean. Eng.* **2021**, *219*, 108273. [CrossRef]
22. Ray, S.; De, S.; Mandal, B.N. Water Wave Scattering by a Bottom-Standing Thick Rectangular Barrier in the Presence of an Ice Cover. *J. Appl. Mech. Tech. Phys.* **2020**, *61*, 400–408. [CrossRef]
23. Gayathri, R.; Kar, P.; Behera, H.; Sahoo, T. Oblique wave scattering by a floating bridge in the presence of a vertical permeable flexible barrier. *J. Offshore Mech. Arct. Eng.* **2021**, *143*, 021701. [CrossRef]
24. De Vita, F.; De Lillo, F.; Bosia, F.; Onorato, M. Attenuating surface gravity waves with mechanical metamaterials. *Phys. Fluids* **2021**, *33*, 047113. [CrossRef]
25. Stoker, J.J. *Water Waves: The Mathematical Theory with Applications*; John Wiley & Sons: New York, NY, USA, 2011; Volume 36.
26. Katsikadelis, J.T. *The Boundary Element Method for Engineers and Scientists: Theory and Applications*; Academic Press: London, UK, 2016.
27. Evans, D.V.; Davies, T.V. *Wave-Ice Interaction*; Stevens Institute of Techology, Davidson Laboratory: Hoboken, NJ, USA, 1968.
28. Sahoo, T. *Mathematical Techniques for Wave Interaction with Flexible Structures*; CRC Press: New York, NY, USA, 2012.
29. Kar, P.; Koley, S.; Sahoo, T. Scattering of surface gravity waves over a pair of trenches. *Appl. Math. Model.* **2018**, *62*, 303–320. [CrossRef]
30. Kar, P.; Sahoo, T.; Behera, H. Effect of Bragg scattering due to bottom undulation on a floating dock. *Wave Motion*, **2019**, *90*, 121–138. [CrossRef]